

Excitation and steepening of ion-acoustic waves in the ionospheric Alfvén resonator

D. Sydorenko,¹ R. Rankin,¹ and K. Kabin^{1,2}

Received 9 March 2010; revised 30 June 2010; accepted 5 August 2010; published 18 November 2010.

[1] A nonlinear two-dimensional fluid model describing excitation of the ionospheric Alfvén resonator by a shear Alfvén wave coming from the magnetosphere is developed. Initially, the plasma is in an equilibrium defined by a balance between the gravity, electric field, and pressure gradient forces. This equilibrium is perturbed when a standing Alfvén wave is excited in the resonator. The nonlinear Lorentz force of the wave creates converging and diverging plasma flows along the geomagnetic field, thus producing compressions and rarefactions in the plasma density. Simulation reveals that density perturbations evolve into ion-acoustic shock waves in a process similar to the nonlinear steepening of sound waves in neutral gases. A shock associated with compression of hydrogen ions propagates faster than a shock associated with compression of oxygen ions. One-dimensional shock-capturing Poisson simulation reveals that the shocks appear as double layers at first, but then they decay into ion-acoustic wave packets. The drop of potential across each shock is negligible at any stage of shock's development, making these shocks unfavorable for auroral electron acceleration.

Citation: Sydorenko, D., R. Rankin, and K. Kabin (2010), Excitation and steepening of ion-acoustic waves in the ionospheric Alfvén resonator, *J. Geophys. Res.*, 115, A11212, doi:10.1029/2010JA015448.

1. Introduction

[2] The interest to nonlinear structures in the Earth magnetosphere, such as shock waves, solitons, and double layers, is related with their particle acceleration effect [Mozer *et al.*, 1980]. The present paper addresses a well known mechanism of formation of such structures, namely the nonlinear wave steepening. Formation of shock waves due to nonlinear steepening of compressive MHD waves, for example, is a well known phenomena in the solar corona, see the review of Warmuth [2007, and the references therein]. Erkaev *et al.* [2001] demonstrated that a pressure pulse produced by a volcanic eruption on Io creates slow MHD waves which propagate toward Jupiter and grow due to the nonlinear steepening. The nonlinear steepening of obliquely propagating inertial Alfvén waves in the near-Earth plasma is studied theoretically and numerically and compared with spacecraft observations by Seyler *et al.* [1995]. The nonlinear steepening of ion-acoustic waves propagating parallel to the geomagnetic field, however, is largely overlooked in the studies of the low-altitude magnetosphere.

[3] The reason why the nonlinear steepening of ion-acoustic waves is usually discarded [Prakash, 1997] may be that this process is not possible due to strong Landau damping if the electron temperature is about the ion tem-

perature [Andersen *et al.*, 1967]. Therefore, the nonlinear steepening is an unlikely mechanism for altitudes below 2000 km, where the electron and ion temperatures are of the same order, 2000–4000 K. At altitudes above 2000 km, however, the electron temperature may be of the order of a few eV (about 20000–30000 K) [Kletzing *et al.*, 1998] and, if the ion temperature stays in the range of a few thousand K, the nonlinear steepening of ion acoustic waves becomes possible.

[4] Various satellites observed double layers and solitary waves in the magnetosphere at different altitudes: Freja at 1700 km [Dovner *et al.*, 1994], FAST at 4000 km [Ergun *et al.*, 1998], S3-3 at 6000 km [Temerin *et al.*, 1982], Polar at 7000 km [Dombeck *et al.*, 2001], Viking at 9700 km [Bostrom *et al.*, 1988]. Such structures are usually accompanied by intense upward ion beams and may be associated with nonlinear electrostatic ion cyclotron or ion acoustic waves. An ion-acoustic double layer, for example, forms if there is an intense current or a flow of electrons relative to ions with the speed comparable with the electron thermal speed [see Hudson and Mozer, 1978, and the references therein]. Although such rapid flows are typical in the auroral acceleration region (altitude of 1–2 Earth radii), they are usually not registered at lower altitudes. The nonlinear structures at these altitudes still may appear as a result of nonlinear evolution of an intense ion-acoustic wave, which occurs even without having the intense parallel electric current.

[5] Montgomery [1967] pointed out that propagation of an ion-acoustic wave is mathematically similar to a nonlinear sound wave in a neutral gas. A sound wave steepens and, under certain conditions, develops into a discontinuity

¹Department of Physics, University of Alberta, Edmonton, Alberta, Canada.

²Now at Department of Physics, Royal Military College of Canada, Kingston, Ontario, Canada

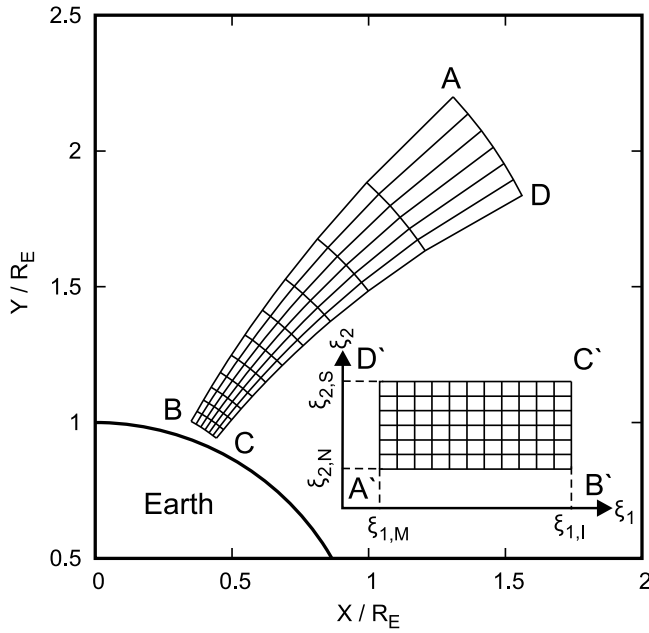


Figure 1. Schematic of the simulated area. Corners A, B, C, and D of the area in the real configuration space correspond to the corners A', B', C', and D' of the rectangle in the dipole coordinate space, respectively.

thus becoming a shock wave [e.g., *Landau and Lifshitz, 1987*]. Steepening of an ion-acoustic wave into a shock is observed both in laboratory plasmas [*Andersen et al., 1967*] and numerical simulations [*White et al., 1974; Kozlov and McKinstrie, 2002*].

[6] In low-altitude magnetosphere, *Sydorenko et al. [2008]* showed that an intense initial density perturbation can be formed by the nonlinear Lorentz force (ponderomotive effect) of a standing Alfvén wave in the ionospheric Alfvén resonator (IAR) [*Polyakov and Rapoport, 1981*]. If a higher harmonics of the resonator is excited, the density perturbations may be formed at altitudes up to about 4000 km, where the top boundary of the resonator is situated. The present paper shows that such perturbations evolve into compressional shock waves. The shock waves propagate upward along the geomagnetic field with the speed equal to the speed of fast or slow ion-acoustic waves in a plasma with multiple warm ion species [*Fried et al., 1971; Kozlov and McKinstrie, 2002*]. Formation of the shock waves in the IAR is demonstrated using a two-dimensional multifluid quasineutral model of low-altitude auroral flux tubes. This model, capable of describing large-scale dynamics of the near-Earth plasma, provides coarse spatial resolution and is not suited for description of sharp discontinuities, which is why these simulations have to be stopped at an early nonlinear stage of shock's development. A much more detailed picture of shock's evolution is obtained with the help of a one-dimensional shock-capturing multifluid electrostatic code. Simulation of a relatively short system, where the electron Debye length is well resolved by the grid, reveals that the ion acoustic shock wave at first appears as a double layer and then decays into a short intense ion-acoustic wave packet, in qualitative agreement with *Hirose et al. [1978]* and *Verheest [1989]*.

[7] The paper is organized as follows. Section 2 describes the two-dimensional numerical model of the near-Earth magnetospheric plasma. In section 3, the nonlinear steepening of ion-acoustic wave structures in magnetospheric simulations is discussed. Issues related with insufficient spatial resolution and numerical artefacts of the magnetospheric model are clarified in section 4 by means of shock-capturing one-dimensional simulation. The one-dimensional model solves the Poisson equation and resolves the electron Debye length. A summary of the results is given in section 5.

2. Model Description

2.1. Alfvén Wave Electromagnetic Field and Plasma Dynamics Equations

[8] A two-dimensional (2-D) model of low-altitude auroral flux tubes discussed below is developed from the IAR model described by *Sydorenko et al. [2008]*. The present model studies nonlinear plasma dynamics induced by Alfvén waves in the near-Earth magnetosphere. It is assumed that the plasma is azimuthally symmetric and the geomagnetic field is dipole. The model uses a 2-D uniform structured grid in dipole coordinates. Directions along and across the geomagnetic field in the meridional plane are resolved. The northern and southern boundaries of the simulated area coincide with geomagnetic field lines (curves AB and CD in Figure 1), the bottom boundary corresponds to a perfectly conducting ionosphere (curve BC in Figure 1), and the top end is open to Alfvén waves (curve AD in Figure 1). The boundary conditions are the same as of *Sydorenko et al. [2008]*, however, the electromagnetic field and the plasma dynamics equations are essentially different.

[9] The present model considers a purely transverse Alfvén wave:

$$\begin{aligned} \frac{\partial E_2}{\partial t} &= -\frac{V_{A,eff}^2}{h_1 h_3} \frac{\partial h_3 B_3}{\partial \xi_1}, \\ \frac{\partial B_3}{\partial t} &= -\frac{1}{h_1 h_2} \frac{\partial h_2 E_2}{\partial \xi_1}, \end{aligned} \quad (1)$$

where the effective Alfvén speed is

$$V_{A,eff}^{-2} = c^{-2} + \sum_{\alpha=O,H} \frac{\mu_0 n_\alpha m_\alpha}{B_E^2},$$

c is the light speed, B_E is the geomagnetic field, m_α and n_α are the mass and the number density of ion species α , subscripts $\alpha = O$ and $\alpha = H$ denote oxygen and hydrogen ions. The dipole coordinates $\xi_{1,2,3}$ are $\xi_1 = \cos \vartheta / r^2$, $\xi_2 = \sin^2 \vartheta / r$, and $\xi_3 = -\varphi$, where $\{r, \vartheta, \varphi\}$ are the ordinary spherical coordinates. The metric factors $h_{1,2,3}$ are $h_2 = r^2 / (\sin \vartheta \sqrt{1 + 3 \cos^2 \vartheta})$, $h_3 = r \sin \vartheta$, and $h_1 = h_2 h_3$. Subscript 1 corresponds to vector components directed along the geomagnetic field line (in the ξ_1 direction), subscript 2 corresponds to vector components normal to the geomagnetic field line in the meridional plane (in the ξ_2 direction), and subscript 3 corresponds to azimuthally directed vector components (in the ξ_3 direction). Below, all vector components directed along the geomagnetic field are referred to as the parallel ones. The wave equations (1) are coupled to the plasma motion through the dynamic equations described below.

[10] Ion velocity across the geomagnetic field (in the meridional plane) corresponds to the inertial ion current:

$$u_{\alpha,2} = \frac{m_\alpha}{eB_E^2} \frac{\partial E_2}{\partial t}, \alpha = O, H, \quad (2)$$

where e is the elementary charge, $e > 0$. The azimuthal ion velocity $u_{\alpha,3} = -E_2/B_E$ is the velocity of drift in crossed wave electric field E_2 and geomagnetic field B_E . The parallel ion velocity is

$$\frac{\partial u_{\alpha,1}}{\partial t} = -[(\mathbf{u}_\alpha \cdot \nabla) \mathbf{u}_\alpha]_1 + \frac{e}{m_\alpha} (E_1 + u_{\alpha,2} B_3) - \frac{1}{m_\alpha n_\alpha h_1} \frac{\partial}{\partial \xi_1} n_\alpha T_\alpha + g_1, \alpha = O, H, \quad (3)$$

where T_α is the ion temperature, g_1 is the parallel acceleration due to the gravity force, and the parallel component of the convective velocity derivative is

$$[(\mathbf{u}_\alpha \cdot \nabla) \mathbf{u}_\alpha]_1 = \frac{u_{\alpha,1}}{h_1} \frac{\partial u_{\alpha,1}}{\partial \xi_1} + \frac{u_{\alpha,2}}{h_2} \frac{\partial u_{\alpha,1}}{\partial \xi_2} + \frac{u_{\alpha,1} u_{\alpha,2}}{2h_1^2 h_2} \frac{\partial h_1^2}{\partial \xi_2} - \frac{u_{\alpha,2}^2}{2h_1 h_2^2} \frac{\partial h_2^2}{\partial \xi_1} - \frac{u_{\alpha,3}^2}{2h_1 h_2^2} \frac{\partial h_3^2}{\partial \xi_1}.$$

[11] The azimuthal electron velocity is the same as that of ions, $u_{e,3} = -E_2/B_E$. Electron motion across the geomagnetic field in the meridional plane is omitted, $u_{e,2} = 0$. The parallel electron velocity is

$$\frac{\partial u_{e,1}}{\partial t} = -[(\mathbf{u}_e \cdot \nabla) \mathbf{u}_e]_1 - \frac{e}{m_e} E_1 - \frac{1}{m_e n_e h_1} \frac{\partial}{\partial \xi_1} n_e T_e + g_1, \quad (4)$$

where m_e , n_e , and T_e are the electron mass, number density, and temperature, respectively, and the parallel component of the convective velocity derivative is

$$[(\mathbf{u}_e \cdot \nabla) \mathbf{u}_e]_1 = \frac{u_{e,1}}{h_1} \frac{\partial u_{e,1}}{\partial \xi_1} - \frac{u_{e,3}^2}{2h_1 h_2^2} \frac{\partial h_3^2}{\partial \xi_1}.$$

The ion densities are calculated via the continuity equations

$$-\frac{\partial n_\alpha}{\partial t} = \frac{1}{h_1 h_2 h_3} \left[\frac{\partial (n_\alpha u_{\alpha,1} h_2 h_3)}{\partial \xi_1} + \frac{\partial (n_\alpha u_{\alpha,2} h_1 h_3)}{\partial \xi_2} \right], \alpha = O, H, \quad (5)$$

while the electron density is obtained from the quasineutrality condition

$$n_e = n_O + n_H. \quad (6)$$

[12] For the sake of simplicity, it is assumed that local values of temperatures of all species do not change with time, i.e., $\partial T_\alpha / \partial t = 0$, where $\alpha = e, O, H$.

2.2. Quasineutral Parallel Electric Field

[13] In order to satisfy condition (6), the divergence of the total electric current must be zero, which results in

$$\frac{\partial}{\partial \xi_1} (J_1 h_2 h_3) = -\frac{\partial}{\partial \xi_2} (J_2 h_1 h_3), \quad (7)$$

where $J_1 = \sum_{\alpha=e,O,H} q_\alpha n_\alpha u_{\alpha,1}$ is the parallel electric current, $J_2 = \sum_{\alpha=O,H} q_\alpha n_\alpha u_{\alpha,2}$ is the transverse electric current, $q_e = -e$ and $q_{O,H} = e$ are the electron and ion charges. The transverse

current is defined by the ion dynamics of the Alfvén wave. With J_2 known, equation (7) becomes an equation for the parallel current J_1 .

[14] The parallel electric field, which creates the parallel current satisfying condition (7), can be obtained by differentiating (7) over time and using equations of ion and electron motion, (3) and (4):

$$E_1 \sum_{\alpha=e,O,H} \frac{n_\alpha e^2}{m_\alpha} = \sum_{\alpha=e,O,H} q_\alpha \left\{ \frac{1}{h_1} \frac{\partial}{\partial \xi_1} \left(\frac{n_\alpha T_\alpha}{m_\alpha} \right) - u_{\alpha,1} \frac{\partial n_\alpha}{\partial t} + n_\alpha [(\mathbf{u}_\alpha \cdot \nabla) \mathbf{u}_\alpha]_1 \right\} - \sum_{\alpha=O,H} \frac{n_\alpha e^2}{m_\alpha} u_{\alpha,2} B_3 + \frac{\partial J_1}{\partial t}. \quad (8)$$

[15] Note, using $\nabla \cdot n \mathbf{u} \mathbf{u} = \mathbf{u} (\nabla \cdot n \mathbf{u}) + n (\mathbf{u} \cdot \nabla) \mathbf{u}$ and the continuity equation, the second and the third terms in the right-hand side of (8) reduce to

$$-u_{\alpha,1} \frac{\partial n_\alpha}{\partial t} + n_\alpha [(\mathbf{u}_\alpha \cdot \nabla) \mathbf{u}_\alpha]_1 = [\nabla \cdot (n_\alpha \mathbf{u}_\alpha \mathbf{u}_\alpha)]_1,$$

which in case of one-dimensional motion is proportional to the parallel gradient of the ram pressure, $\nabla m_\alpha n_\alpha u_{\alpha,1}^2$.

2.3. Initial Equilibrium State

[16] The presence of the thermal pressure and gravity forces in the equations of parallel motion (3) and (4) requires an equilibrium state as an initial condition for the simulation. Such an equilibrium is produced as follows. First, the oxygen and ion densities are assumed to be:

$$n_O(r)|_{t=0} = n_O^0 \exp \left[-\frac{r - R_E - h_I}{l_1 + l_2 \tanh \frac{(r - R_E - h_I)}{l_3}} \right], \quad (9)$$

$$n_H(r)|_{t=0} = n_H^0 \left(\frac{R_E + h_I}{r} \right)^p,$$

where $n_O^0 = 3.2 \times 10^{11} \text{ m}^{-3}$, $n_H^0 = 7 \times 10^8 \text{ m}^{-3}$, $R_E = 6380 \text{ km}$ is the Earth radius, $h_I = 400 \text{ km}$ is the altitude of the top ionospheric layer, $l_1 = 130 \text{ km}$, $l_2 = 325 \text{ km}$, $l_3 = 2400 \text{ km}$, and $p = 3$. Functions (9) approximate densities provided by the International Reference Ionosphere model (available at http://omniweb.gsfc.nasa.gov/vitmo/iri_vitmo.html). The ion density profiles are shown in Figure 2a. With densities (9) and the dipole geomagnetic field (shown in Figure 2b), the Alfvén speed has a nonmonotonic profile shown in Figure 2c. Note that according to this profile, the IAR is formed between the ionosphere and the altitude of about 4000–5000 km, where the upward gradient of the Alfvén speed is maximal.

[17] Second, the oxygen ion temperature is set constant $T_O = 0.2 \text{ eV}$ throughout the whole simulation area. This assumption allows to find the parallel equilibrium electric field from the equation of momentum balance for oxygen ions:

$$E_1 = \frac{T_O}{e n_O h_1} \frac{\partial n_O}{\partial \xi_1} - \frac{m_O}{e} g_1.$$

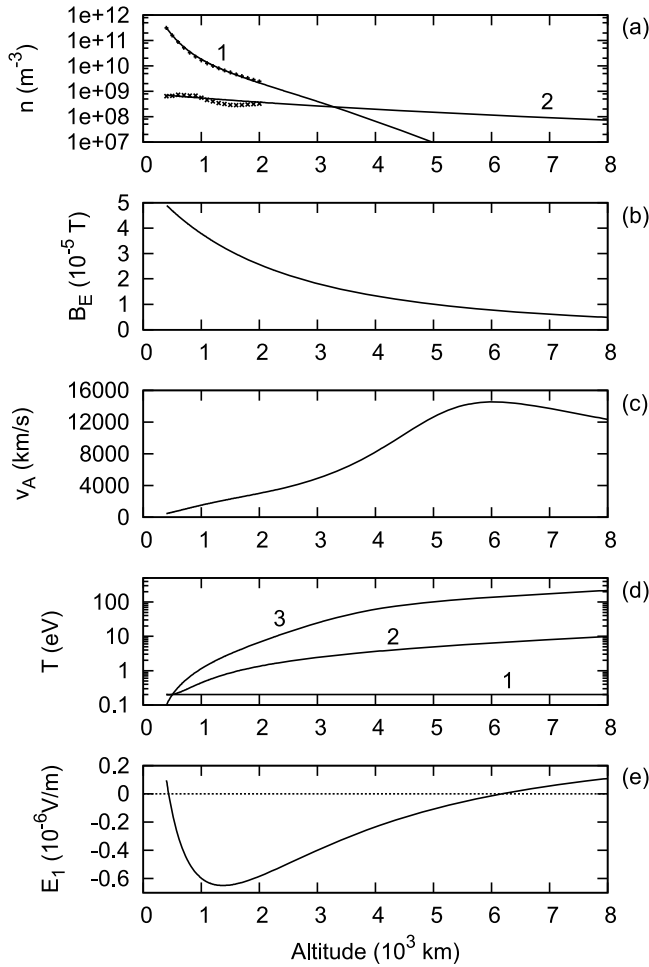


Figure 2. Initial profiles of (a) ion number density, (b) geomagnetic field, (c) Alfvén speed, (d) temperature, and (e) parallel electric field. In Figure 2a, curves 1 and 2 are for oxygen and hydrogen, respectively, markers show values obtained with the online International Reference Ionosphere model (available at http://omniweb.gsfc.nasa.gov/vitmo/iri_vitmo.html). In Figure 2d, curves 1, 2, and 3 are for oxygen, hydrogen, and electrons, respectively. The ionospheric boundary is at altitude of 400 km.

The profile of the parallel electric field in the equilibrium is shown in Figure 2e.

[18] Finally, hydrogen ion and electron temperatures are prescribed at the ionospheric boundary $\xi_1 = \xi_{1,i}$: $T_H(\xi_{1,i}) = 0.2$ eV and $T_e(\xi_{1,i}) = 0.1$ eV. In the rest of the system, these temperatures are determined by the corresponding momentum balance equations:

$$\begin{aligned} \frac{\partial}{\partial \xi_1} n_H T_H &= h_1 n_H (eE_1 + m_H g_1), \\ \frac{\partial}{\partial \xi_1} n_e T_e &= h_1 n_e (-eE_1 + m_e g_1). \end{aligned}$$

[19] The electron and ion temperature profiles are shown in Figure 2d. Note that hydrogen and electron temperatures exhibit monotonic growth similar to temperature profiles used, e.g., from *Chaston et al.* [2004]. It should be noted, however, that some data show a much slower electron tem-

perature growth (within 1–5 eV) up to altitudes of 8000 km [*Kletzing et al.*, 1998]. Besides, kinetic model of equilibrium of anisotropic plasmas developed by *Ergun et al.* [2000] predicts a stepwise increase of the electron temperature at altitudes of several thousand kilometers instead of the smooth growth. So, the question of how realistic are the temperature profiles obtained above remains open.

2.4. Discussion of the Numerical Scheme

[20] The continuity equation for ions (5) is rewritten for the density logarithm $\ln(n_\alpha)$ and is solved using a semi-Lagrangian method described by, e.g., *Staniforth and Cote* [1991]. The advection is described by a three-time-level scheme, i.e., the values of density in the nodes of the grid at time t^{n+1} are calculated using the nodal density values at time t^{n-1} and velocity values at time t^n , superscripts n and $n \pm 1$ denote time t^n and $t^{n \pm 1} = t^n \pm \Delta t$ when a variable with the superscript was calculated (Δt is the time step). The 2-D-interpolation of the ion density in space is performed using cubic Hermite splines with limiters as described by *Carlson and Fritsch* [1985], which preserves monotonicity of the density profile. The use of the logarithm of the density ensures its positivity.

[21] The three-time-level advection provides the advanced densities n_α^{n+1} before finding the advanced transverse ion velocities $u_{\alpha,2}^{n+1}$. With known n_α^{n+1} , equations for the transverse electromagnetic field (1) and transverse ion dynamics (2) in implicit finite difference form produce a three-diagonal system of linear equations with respect to the updated wave magnetic field B_3^{n+1} . After the system is solved, the advanced transverse electric field E_2^{n+1} and ion velocity $u_{\alpha,2}^{n+1}$ are readily calculated.

[22] The advanced parallel current J_1^{n+1} is calculated from the finite difference equivalent of (7) when the updated transverse current $J_2^{n+1} = \sum_{\alpha=O,H} q_\alpha n_\alpha^{n+1} u_{\alpha,2}^{n+1}$ is found. With known J_1^{n+1} and n_α^{n+1} , the updated parallel quasineutral electric field E^{n+1} is found from the implicit finite difference form of (8). Finally, the parallel flow velocities are updated using the implicit finite difference form of (3) and (4).

[23] The implicit quasineutral semi-Lagrangian algorithm described above can be relatively easily transferred to non-uniform grids. No sign of numerical instability appears in simulations covering 4 minutes of the magnetospheric plasma evolution. The semi-Lagrangian advection implemented in the present model, however, is not conservative and shows noticeable numerical diffusion, which affects position of the front and reduces the amplitude of nonlinear waves [*Priestley*, 1993]. Moreover, even though advection itself does not introduce spurious maxima or minima into the density profiles of the plasma species, the parallel electric current calculated as a difference between the electron and ion fluxes may contain spurious oscillations.

[24] In order to avoid nonphysical effects introduced by the numerical method, simulations are carried out with different spatial resolution (grid cell size) and the convergence between the results of these simulations is monitored. A simulation is stopped once it develops oscillatory structures with the spatial scale proportional to the size of the grid cell. Usually this happens soon after the beginning of the nonlinear stage, as described in section 3. Furthermore, the conclusions made on the basis of simulations with the 2-D

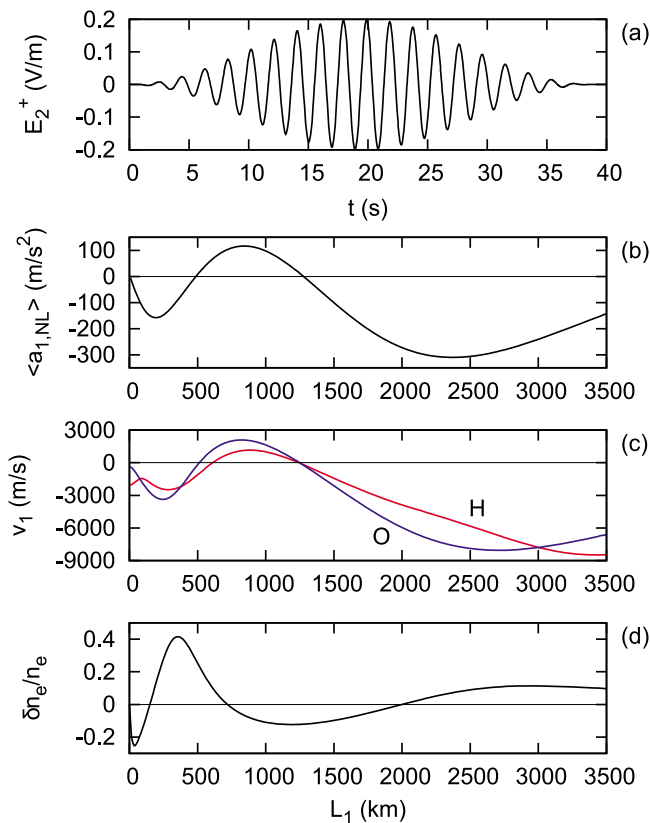


Figure 3. Formation of density perturbation when the first IAR harmonic is excited. (a) Electric field of the incoming wave versus time in the middle of the magnetospheric boundary. Profiles of (b) average acceleration due to the nonlinear force, (c) ion velocity along the geomagnetic field, and (d) relative plasma density perturbation. Positive values in Figures 3b and 3c are directed downward, toward the ionosphere $L_1 = 0$. Averaging in Figure 3b is performed over the wave period starting at $t = 18.4$ s. Ion velocity in Figure 3c and relative density perturbation in Figure 3d are obtained at $t = 39.6$ s. In Figure 3c, the hydrogen and the oxygen curves have labels H and O, respectively. The relative density perturbation in Figure 3d is calculated as $n_e(t)/n_e(0) - 1$, where $n_e(t)$ is the plasma density at time t and $n_e(0)$ is the initial plasma density. The amplitude of the driving Alfvén wave packet is $E_2^+ = 0.2$ V/m. The numerical grid has 400 cells in the parallel direction.

IAR model are verified in section 4 using a one-dimensional shock-capturing model.

2.5. Simulation Parameters

[25] The simulation area is defined by positions of three corner points: the southern ionospheric corner (C in Figure 1) is at latitude 69.68° and altitude 400 km, the northern ionospheric corner (B in Figure 1) is at latitude 70° , the southern high-altitude corner (D in Figure 1) is at latitude 58° . The width of the ionospheric boundary (segment BC in Figure 1) is 39.2 km, the width of the high-altitude boundary (segment AD in Figure 1) is 148.7 km, the distance between the mid-points of these boundaries calculated along the geomagnetic field line is 9356 km. The computational grid has 60 cells in the ξ_2 -direction and from 400 to 1600 cells in the ξ_1 -

direction. In case of 400 cells, the grid cell size in the direction parallel to the geomagnetic field varies from 6944 m at the low-altitude end to 94544 m at the high-altitude end. The time step $\Delta t = 0.00267$ s is the maximal value satisfying an equivalent of Courant's condition for Alfvén waves $\Delta t < h_1 \Delta \xi_1 / V_{A,eff}$ everywhere in the simulation area. In case of 1600 cells, the parallel grid cell size varies from 1736 m to 23635 m, the time step is $\Delta t = 0.00067$ s.

3. Nonlinear Ion-Acoustic Waves in Quasineutral Large-Scale Simulations of Magnetospheric Plasmas

3.1. Formation of Density Perturbation in the IAR

[26] A simulation is performed where a downward propagating Alfvén wave packet enters the system through the high-altitude open-end boundary. The wave packet consists of 20 wave periods with the frequency 0.515 Hz corresponding to the first IAR harmonic. The wave packet envelope is similar to the one used by *Sydorenko et al.* [2008], with a maximal transverse electric field amplitude $E_2^+ = 0.2$ V/m, as shown in Figure 3a.

[27] The transverse profile of the wave packet is Gaussian, with a maximum in the middle of the high-altitude boundary. Note, since the density perturbations of interest are the strongest where the driving Alfvén wave is the strongest, the present paper considers only profiles along the middle geomagnetic field line of the simulation domain. Also, starting from Figure 3, distance L_1 along the geomagnetic field line calculated upward from the ionospheric end is used as the position coordinate for the profiles unless otherwise stated, as from *Sydorenko et al.* [2008]. The reason for this choice is that such distance is required for calculation of the speed of wave propagation along the geomagnetic field.

[28] The wave packet excites the first harmonic of the IAR. The nonlinear Lorentz (ponderomotive) force of the standing wave (see the profile in Figure 3b) creates plasma flows converging toward a point with $L_1 \approx 500$ km and diverging away from a point with $L_1 \approx 1250$ km (see Figure 3c). After just 40 seconds, these flows produce significant large-scale modification of the plasma density, as shown in Figure 3d. *Sydorenko et al.* [2008] suggested that such process may be responsible for formation of density cavities in the low-altitude magnetosphere. The plasma from *Sydorenko et al.* [2008] was cold. The present model accounts for thermal effects and reveals a much more complex plasma dynamics.

[29] The aforementioned density modification increases the gradient of the electron pressure at $L_1 \approx 550$ km, which results in the local increase of the parallel electric field, in agreement with equation (8). This electric field perturbation grows with time and acquires the form of a negative (directed upward) spike of the parallel electric field propagating upward (see evolution of the spike with label S (“slow”) in Figure 4).

[30] The nonlinear Lorentz force of the Alfvén wave packet does not depend on the ion mass, while the force of the parallel electric field does. Since hydrogen ions are much lighter than the oxygen ones, there is a significant difference between the motion of the two ion species when the Alfvén wave decays (compare velocity profiles for hydrogen and oxygen ions in Figure 5a). As a result, modification of the

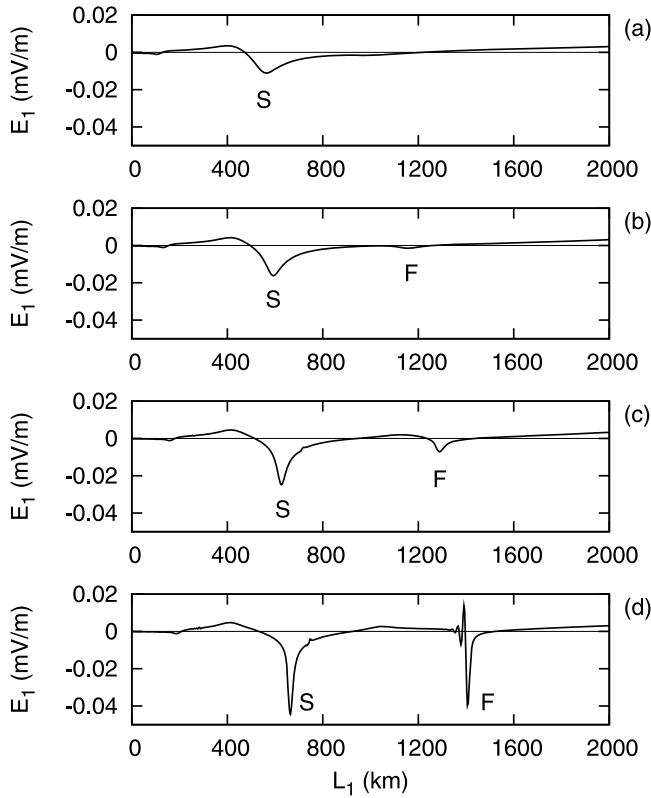


Figure 4. Temporal evolution of the parallel electric field profile in the simulation with the amplitude of the driving Alfvén wave packet $E_2^+ = 0.2\text{V/m}$. (a–d) Values obtained at times $t_a = 81.5\text{s}$, $t_b = 91.2\text{s}$, $t_c = 100.9\text{s}$, and $t_d = 110.6\text{s}$. The oxygen (slow) ion-acoustic wave structure has label S. The hydrogen (fast) ion-acoustic wave structure has label F. Wave structures S and F correspond to the wave structures with the same labels in Figure 4a of Figure 8. Positive field values are directed downward, toward the ionosphere at $L_1 = 0$. The numerical grid has 1600 cells in the parallel direction.

hydrogen ion density profile is different from that of the oxygen ions (compare profiles in Figure 5b). In particular, by $t \approx 80\text{s}$, hydrogen ion flows converging toward $L_1 \approx 1000\text{ km}$ amplify the hydrogen ion density gradient (and, due to quasineutrality, the electron density gradient) at $L_1 \approx 1150\text{ km}$ and produce another electric field perturbation (labeled F (“fast”) in Figures 4 and 5c). This perturbation propagates upward at a much higher speed than the other one.

[31] Profiles of the aforementioned wave structures obtained in simulations with different spatial resolution in the parallel direction are very close to each other during the first 100 seconds, as it is shown in Figure 6a. After this time, the value of the parallel electric field maximum in spikes S and F grows faster in a simulation with a finer grid. This is a reasonable behavior because limitation of the gradient by a coarse grid is an unwanted numerical effect. However, by $t \approx 120\text{s}$, noticeable oscillatory wakes appear behind both spikes (oscillations following spike F are seen in Figure 4d). The wavelength of these oscillations is about 8 grid cells regardless of what the cell size is

(see Figure 6b), which allows to conclude that they are of numerical rather than physical origin. Because of this, the simulation is stopped at $t = 120\text{s}$.

3.2. Dispersion Equation of Ion-Acoustic Waves

[32] The nature of perturbations described above becomes clear if one compares their dispersion with the dispersion of ion-acoustic waves. The ion-acoustic dispersion equation can be obtained as a result of a standard procedure, where a harmonic perturbation is substituted into linearized equations of motion (3) and (4), ion continuity equations (5), and equation for the quasineutral parallel electric field (8). It is further assumed that (1) the quasineutrality (6) holds for electron and ion density perturbations, (2) there is no motion in transverse directions, (3) contributions of curvature and temperature gradients can be neglected. It is important to account for the flows of electrons and ions. Omitting the lengthy but straightforward algebra, the dispersion relation of ion-acoustic waves is

$$-v_{ph} + 2u_{e,1} = \sum_{\alpha=O,H} \frac{n_{\alpha} m_e}{m_{\alpha} n_e} \frac{2u_{e,1} + v_{ph} (v_{ph}^2 + u_{\alpha,1} v_{ph} - u_{e,1}^2 - u_{\alpha,1}^2 - 1)}{v_{ph} (v_{ph} - u_{\alpha,1}) - v_{\alpha,th}^2}, \quad (10)$$

where v_{ph} is the wave phase velocity in the laboratory frame, $u_{e,1}$, $u_{H,1}$, and $u_{O,1}$ are the electron, hydrogen and oxygen flow velocities in the laboratory frame, $v_{H,th}^2 = T_H/m_H$ and

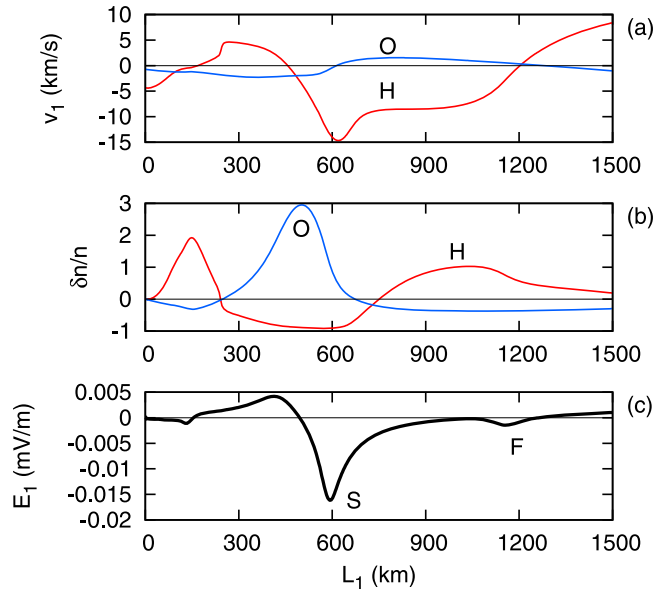


Figure 5. Difference between formation of the slow and the fast wave. Profiles of the (a) parallel ion flow velocity, (b) relative ion density perturbation, and (c) parallel electric field. In Figures 5a and 5b, the hydrogen and the oxygen curves have labels H and O, respectively. In Figure 5c, the slow and the fast ion-acoustic wave structures have labels S and F, respectively. Figures 5a–5c are obtained at time $t = 91.2\text{s}$. The amplitude of the driving Alfvén wave packet is $E_2^+ = 0.2\text{V/m}$. The numerical grid has 1600 cells in the parallel direction.

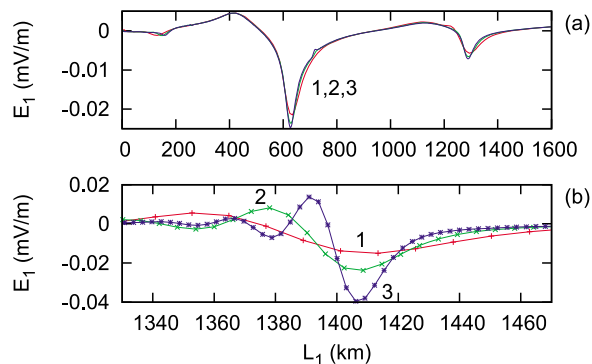


Figure 6. Parallel electric field profiles in magnetospheric simulations with $E_2^+ = 0.2\text{V/m}$, where the numerical grid has 400 (curves 1), 800 (curves 2), and 1600 (curves 3) cells in the parallel direction. (a) Profiles are obtained at $t = 100.9\text{s}$. (b) Profiles are obtained at $t = 110.6\text{s}$. Markers in Figure 6b represent electric field in the nodes of the grid.

$v_{O,th}^2 = T_O/m_O$ are thermal speeds of hydrogen and oxygen ions, the aforementioned velocities are normalized by the electron thermal velocity $v_{e,th} = (T_e/m_e)^{1/2}$. In general, equation (10) has 5 roots. In the absence of the flows, a trivial root $v_{ph} = 0$ corresponds to a stationary state. In addition, two pairs of symmetric (positive and negative) roots describe slow and fast ion-acoustic waves propagating in both directions [Fried et al., 1971; Kozlov and McKinstrie, 2002]. Below, the roots of (10) are referred to using ascending order, starting with the largest in magnitude negative root.

[33] Fast plasma flows may significantly modify dispersion of ion-acoustic waves if the velocities of these flows (Figure 7d) are comparable with local thermal speeds (Figure 7e). In Figure 7a, profiles of phase velocities are given for the initial equilibrium state. With time, profiles of hydrogen and oxygen ion number densities become strongly perturbed (see Figure 7c) and rapid flows develop (see Figure 7d) due to both the nonlinear Lorentz force of the Alfvén wave and the aforementioned waves with intense parallel electric fields. As a result, local values of the phase velocities of ion-acoustic waves deviate strongly from their initial values (compare Figure 7b with Figure 7a).

[34] The dispersion of waves obtained in the simulation can be checked by comparing the wave propagation velocities with theoretical values given by equation (10). Note that the roots of (10) change constantly in space and time. In Figure 8a, the electric field along the middle geomagnetic field line is plotted as a function of coordinate L_1 and time t . Two wave structures selected for comparison are labeled S and F. In Figure 8b, trajectories of two test particles are plotted in the $L_1 - t$ phase plane. Test particle F propagates with the local phase velocity of the upward propagating fast ion-acoustic wave [the first root of the dispersion equation (10)]. Test particle S propagates with the local phase velocity of the upward propagating slow ion-acoustic wave [the second root of the dispersion equation (10)]. There is an excellent agreement between the trajectories of the test particles and the wave structures. Therefore, the wave structures observed in the simulation and shown in Figure 4 can be conclusively identified as the ion-acoustic waves.

3.3. Nonlinear Wave Steepening

[35] A detailed evolution of the parallel electric field spike, which has label S in Figure 4 and Figure 8a, is shown in Figure 9. The spike moves upward with the velocity of the slow ion-acoustic wave. Below, this structure is referred to as an oxygen shock wave (the term “shock” is used because of the reasons described below). The oxygen shock wave is a compressional perturbation of the oxygen ion density, that is the density behind the shock is higher than the density in front of the shock. With time, the parallel spatial scale of the density perturbation decreases (see Figure 9a), which increases the density gradient and the parallel electric field (see Figure 9b). This process resembles formation of a shock wave due to the nonlinear steepening

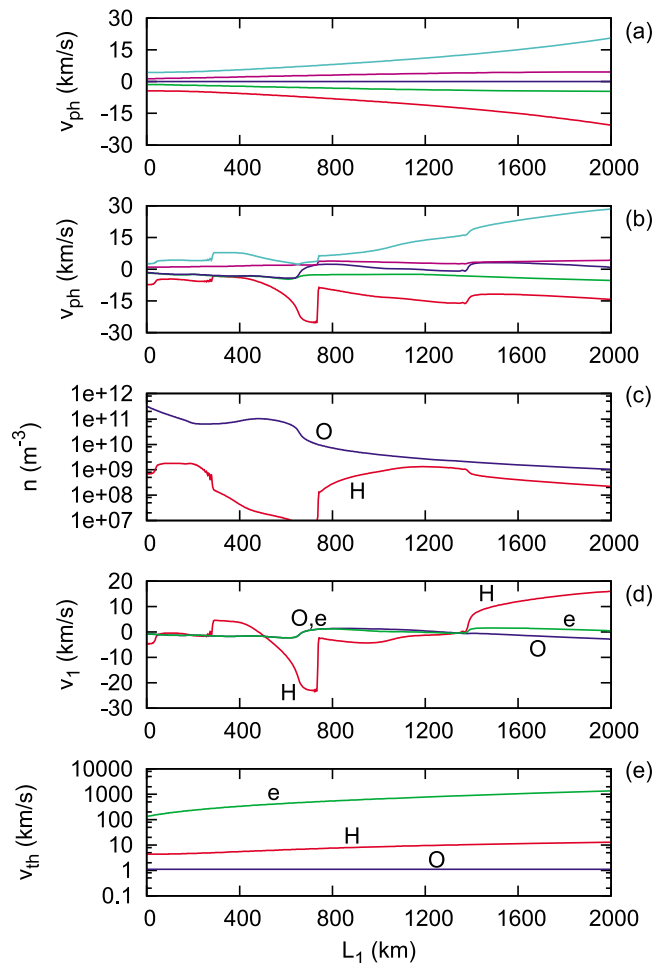


Figure 7. Effect of electron and ion flows and density modification on the dispersion of ion-acoustic waves. (a) Initial profiles of ion-acoustic phase velocities (roots of equation (10)). Final profiles of (b) phase velocities, (c) densities, (d) flow velocities obtained at time $t = 108.6\text{s}$. (e) Profiles of thermal speed. In Figures 7c–7e, curves for electrons, hydrogen ions, and oxygen ions have labels e, H, and O, respectively. In Figures 7a, 7b, and 7d, positive velocity values are directed downward, toward the ionosphere at $L_1 = 0$. The amplitude of the driving Alfvén wave packet is $E_2^+ = 0.2\text{V/m}$. The numerical grid has 1600 cells in the parallel direction.

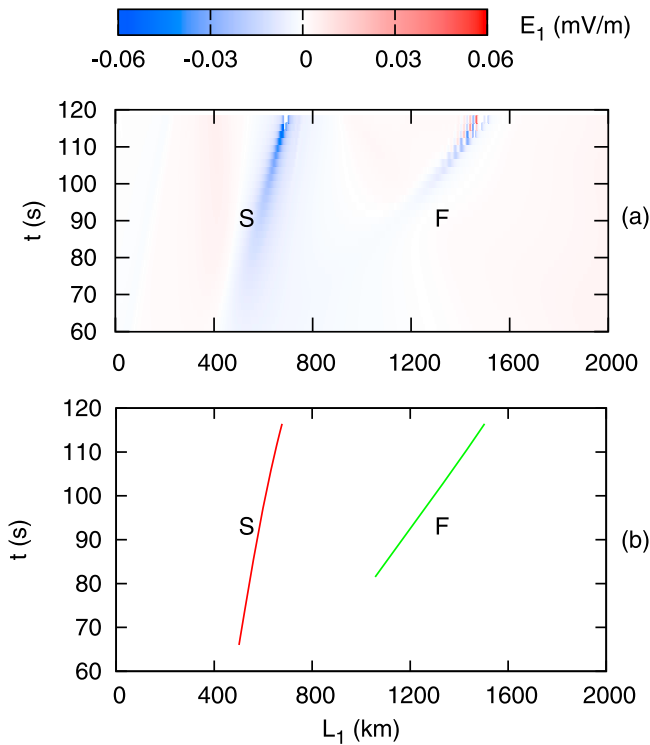


Figure 8. Verification of dispersion of ion-acoustic wave packets observed in simulation with the driving Alfvén wave packet’s amplitude $E_2^+ = 0.2\text{V/m}$ and the numerical grid with 1600 cells in the parallel direction. (a) The color map represents evolution of the parallel electric field profile in time (the vertical axis). Perturbations S and F are the slow and the fast ion-acoustic wave structures labeled S and F in Figure 4. (b) Trajectories of test particles in “coordinate-time” phase space. The velocities of test particles S and F are equal to the local phase velocities of the slow and fast ion-acoustic wave propagating upward, respectively. In both Figures 8a and 8b, the ionospheric boundary is at $L_1 = 0$.

of a sound wave in gas dynamics [Landau and Lifshitz, 1987]. Note that in front of the oxygen shock wave, the oxygen ion flow is directed toward the wave, as shown in Figure 9c. Therefore, in the frame moving with the oxygen shock wave, the oxygen ion flow before the shock is supersonic, while behind the wave the flow is subsonic. This is a characteristic property of a shock wave [Landau and Lifshitz, 1987].

[36] Consider another wave structure, which has label F in Figure 4 and Figure 8a. This is a compressional perturbation of hydrogen ions (see Figure 10a). It propagates with the phase velocity of the fast ion-acoustic wave. Below, this structure is referred to as the hydrogen shock wave. Detailed evolution of the hydrogen shock wave is similar to the evolution of the oxygen one (compare Figure 10 with Figure 9). The difference is that it is the hydrogen ion flow which is supersonic before and subsonic after the hydrogen shock wave (see Figure 10c).

[37] Due to the presence of dynamically changing flows, at some locations and times the roots of the dispersion equation (10) for the ion-acoustic waves may become complex. However, no correlation between the complex

roots and the transformation of initially smooth density perturbations into steep shock waves was found. Also, the relative drift of electrons and ions is much slower than the electron thermal speed. In fact, in the absence of transverse currents, the quasineutrality condition ensures that the total electron current is zero. Thus, formation of the shock waves in the present model is not related to the ion-ion two-stream instability [Wahlund et al., 1992] and the current driven instability [Quon and Wong, 1976; Sato and Okuda, 1981; Foster et al., 1988; Rietveld et al., 1991].

[38] Since ion-acoustic waves in the simulation exhibit nonlinear behavior, it is instructive to investigate the effect of the wave amplitude. Test runs with different values of the amplitude of the driving Alfvén wave reveal that, on one hand, the speed of wave propagation weakly depends on the wave amplitude. On the other hand, if the wave packet amplitude is below some threshold value (0.1V/m for the parameters of the present simulation), shock waves do not develop during 240 seconds of system evolution, as shown in Figures 11a ($E_2^+ = 0.05\text{V/m}$) and 11b ($E_2^+ = 0.1\text{V/m}$). Simulations with $E_2^+ = 0.12\text{V/m}$ (Figure 11c) and $E_2^+ = 0.14\text{V/m}$ (Figure 11d), where the shock waves are observed, are stopped earlier than at 240 seconds, once the oscillatory wakes appear.

[39] The nonlinear wave steepening may not occur because of the Landau damping if the electron and ion temperatures are of the same order, which is usually the case in the real magnetosphere for altitudes below 2000 km.

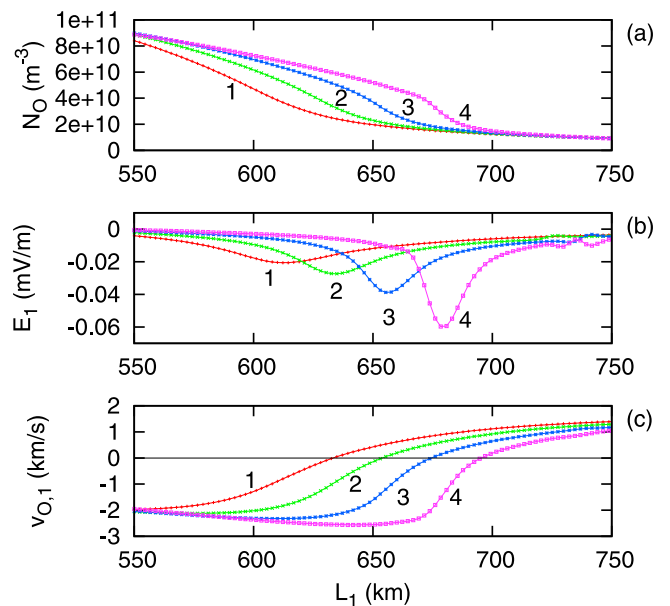


Figure 9. Steepening of a slow ion-acoustic wave. Profiles of (a) oxygen ion density, (b) parallel electric field, and (c) parallel oxygen ion flow velocity in the laboratory frame. Curves 1, 2, 3, and 4 are obtained at times $t_1 = 97\text{s}$, $t_2 = 102.8\text{s}$, $t_3 = 108.6\text{s}$, and $t_4 = 114.4\text{s}$, respectively. In Figures 9b and 9c, negative values are directed upward, away from the ionosphere at $L_1 = 0$. Markers denote values in the nodes of the numerical grid. The driving Alfvén wave packet’s amplitude is $E_2^+ = 0.2\text{V/m}$, the grid has 1600 cells in the parallel direction.

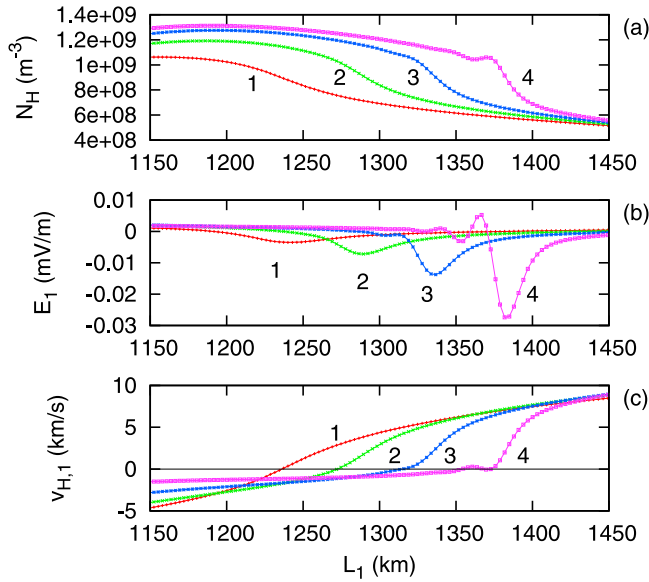


Figure 10. Steepening of a fast ion-acoustic wave. Profiles of (a) hydrogen ion density, (b) parallel electric field, and (c) parallel hydrogen ion flow velocity in the laboratory frame. Curves 1, 2, 3, and 4 are obtained at times $t_1 = 97$ s, $t_2 = 100.9$ s, $t_3 = 104.8$ s, and $t_4 = 108.6$ s, respectively. In Figures 10b and 10c, negative values are directed upward, away from the ionosphere at $L_1 = 0$. Markers denote values in the nodes of the numerical grid. The driving Alfvén wave packet’s amplitude is $E_2^+ = 0.2$ V/m, the grid has 1600 cells in the parallel direction.

Simulations shown in the present paper are carried out with the first IAR harmonic, which excites the density perturbations at a relatively low altitude, about 1000 km. The first harmonic is chosen because, first, it produces a converging plasma flow in one location only, and, therefore, only two shock waves appear which do not overlap and are easy to trace. Second, the numerical grid provides a much better resolution at lower altitudes. If a higher IAR harmonic is excited, it will produce converging plasma flows in multiple locations, including the altitude range from 2000 km to about 4000 km (the top IAR boundary). In the present model, the difference between shocks excited at lower and higher altitudes will be mostly quantitative. Nevertheless, it is important to keep in mind that IAR harmonics with higher numbers are better candidates to produce density perturbations which may evolve into nonlinear shock waves.

4. Nonlinear Ion-Acoustic Waves in One-Dimensional Simulations Resolving the Electron Debye Length

[40] In the simulation described in the previous section, the parallel grid size is of the order of 2–3 km at altitudes of 1–2 thousand kilometers, which exceeds the local value of the electron Debye length (0.1 m–1 m) by several orders of magnitude. On one hand, such coarse resolution is sufficient to describe large-scale dynamics of the magnetospheric plasma, on the other hand, it limits the parallel electric field in the shocks significantly. Moreover, the numerical scheme

of the 2-D IAR model is not the best for description of shock waves, as discussed above.

[41] A correct description of the process of nonlinear ion-acoustic wave steepening must (1) resolve the Debye length, (2) calculate the electrostatic potential from the Poisson equation, and (3) describe sharp discontinuities without introducing spurious oscillations. In order to demonstrate the nonlinear evolution of an ion-acoustic wave unobscured by the limitations of the large-scale quasineutral model, a simple one-dimensional (1-D) multifluid numerical model is applied, as described below.

[42] The model considers a uniform 1-D plasma consisting of electrons, hydrogen and oxygen ions. The plasma is periodical with the period length \mathcal{H} . The model includes equations for the density, momentum, and energy for the three species in the conservative form ($\alpha = e, O, H$):

$$\frac{\partial n_\alpha}{\partial t} + \frac{\partial}{\partial x}(n_\alpha v_\alpha) = 0, \quad (11)$$

$$\frac{\partial n_\alpha v_\alpha}{\partial t} + \frac{\partial n_\alpha v_\alpha^2}{\partial x} = -\frac{n_\alpha q_\alpha}{m_\alpha} \frac{\partial \Phi}{\partial x} - \frac{1}{m_\alpha} \frac{\partial}{\partial x}(n_\alpha T_\alpha), \quad (12)$$

$$\frac{\partial n_\alpha T_\alpha}{\partial t} + \frac{\partial n_\alpha T_\alpha v_\alpha}{\partial x} = -\frac{2}{3} n_\alpha T_\alpha \frac{\partial v_\alpha}{\partial x}, \quad (13)$$

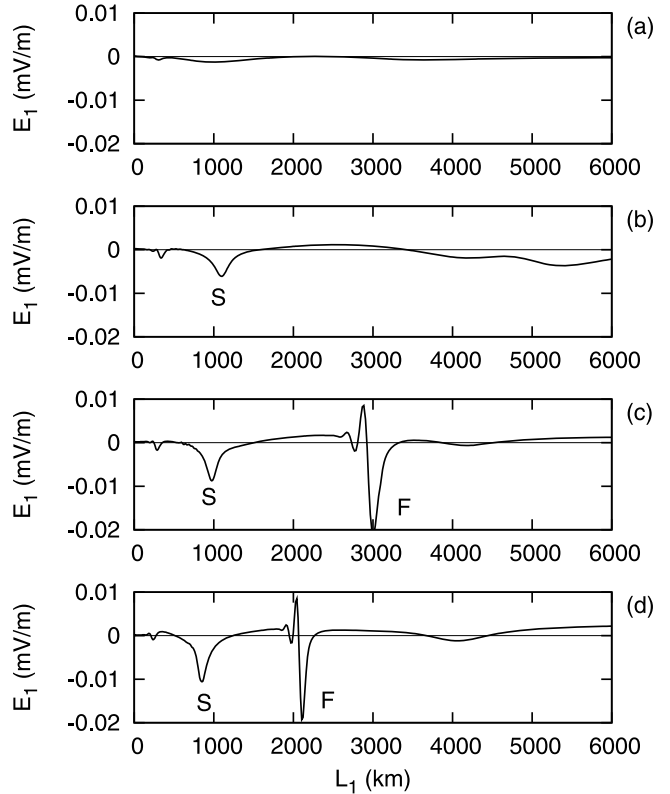


Figure 11. Final parallel electric field profiles for different values of the amplitude of the driving Alfvén wave packet. (a) Values obtained at time $t_a = 237.5$ s with the wave amplitude $E_{2,a}^+ = 0.05$ V/m. (b) Values obtained at $t_b = 237.5$ s with $E_{2,b}^+ = 0.1$ V/m. (c) Values obtained at $t_c = 201.9$ s with $E_{2,c}^+ = 0.12$ V/m. (d) Values at $t_d = 166.3$ s with $E_{2,d}^+ = 0.14$ V/m. Positive field values are directed downward, toward the ionosphere at $L_1 = 0$. The numerical grid has 400 cells in the parallel direction.

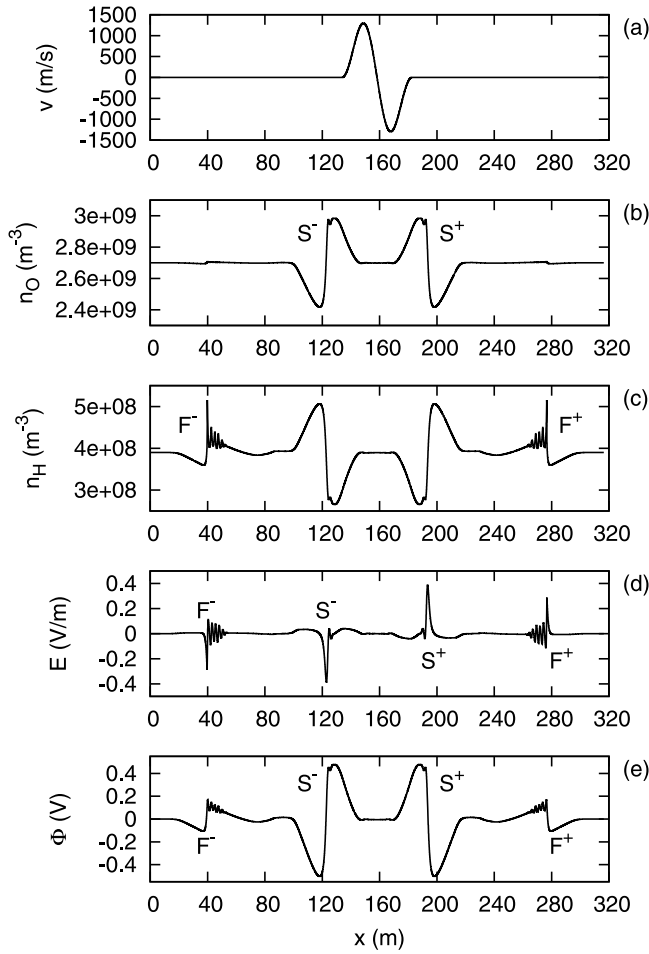


Figure 12. Simulation of nonlinear ion-acoustic waves with Poisson equation. (a) Profile of initial perturbation of flow velocity. Profiles of (b) oxygen ion density, (c) hydrogen ion density, (d) electric field, and (e) electrostatic potential. Labels S^\pm and F^\pm denote oxygen (slow) and hydrogen (fast) ion-acoustic waves propagating in the positive and negative x -directions, respectively. Figures 12b–12e are obtained at time $t = 0.00648$ s. The numerical grid has 32000 cells.

and the Poisson equation

$$\frac{\partial^2 \Phi}{\partial x^2} = -\frac{1}{\epsilon_0} \sum_{\alpha=e,O,H} q_\alpha n_\alpha,$$

where x is the spatial coordinate, v is the velocity, Φ is the electrostatic potential, the rest of the variables is the same as in the 2-D model described in section 2. Equation (13) corresponds to adiabatic compression of monatomic ideal gas with $\gamma = 5/3$. Equations (11)–(13) are solved using a flux-corrected transport (FCT) algorithm proposed by *Boris and Book* [1973], which is a proven method to solve shock problems. The numerical scheme considers the density, momentum, velocity, temperature, and potential on the same grid and at the same moments of time. As a result, time advancing includes iterations. The numerical scheme is described and studied in section II.A of *Rambo and Denavit* [1991]. This algorithm is stable and the iterations converge

when $\omega_{pe} \Delta t < 1$ and $\Delta x > \Delta t (\gamma T_e / m_e)^{1/2}$. Unfortunately, this model is numerically very expensive and cannot be applied to large simulation domains stretching for millions of Debye lengths.

[43] A test simulation is carried out with the following initial plasma parameters: $n_e = 3.09 \times 10^9 \text{ m}^{-3}$, $n_H = 3.9 \times 10^8 \text{ m}^{-3}$, $n_O = 2.7 \times 10^9 \text{ m}^{-3}$, $T_e = 5.6 \text{ eV}$, $T_H = 1.2 \text{ eV}$, $T_O = 0.2 \text{ eV}$. These values are close to the parameters of plasma in the magnetospheric model at $L_1 \approx 1400 \text{ km}$, where the fast ion-acoustic wave (the one with label F in Figure 4 and Figure 8) becomes significant. The 1-D system of length $\mathcal{H} = 316.5 \text{ m}$ is divided into 32000 cells of size $\Delta x = \lambda_{De} / 32 \approx 9.89 \times 10^{-3} \text{ m}$, where $\lambda_{De} = (\epsilon_0 T_e / n_e e^2)^{1/2}$ is the electron Debye length. The time step is $\Delta t = \omega_{pe}^{-1} / (2^{1/2} 32) \approx 7.046 \times 10^{-9} \text{ s}$, where $\omega_{pe}^2 = n_e e^2 / \epsilon_0 m_e$ is the electron plasma frequency. In order to initiate ion-acoustic waves, all plasma components have an initial velocity perturbation as shown in Figure 12a.

[44] The initial velocity perturbation compresses plasma in the middle of the system, like the nonlinear Lorentz force does in the IAR. The compressed area emits two pairs of ion-acoustic waves propagating symmetrically rightward and leftward: slow waves associated with the compression of oxygen (labeled S^+ and S^- in Figures 12b and 12d), and fast waves associated with the compression of hydrogen (labeled F^+ and F^- in Figures 12c and 12d). These waves are similar to perturbations S and F in the simulation of the magnetospheric plasma (see Figures 4 and 8a). The waves steepen and become oxygen (slow) and hydrogen (fast) shocks.

[45] Initially, the electric field in the shocks has a shape of a unipolar spike, as in a double layer. The electric field is directed along the direction of the shock propagation. The double layer pattern, however, does not hold for long. Soon oscillatory trails start growing behind the shock fronts and the amplitude of the spikes gradually decays. The maximal electric field in the oxygen shock S^+ , registered while the double-layer pattern is dominant, is 0.75 V/m at time $t = 0.0123 \text{ s}$, the width of the double-layer electric field spike (calculated at the half of spike's amplitude) is about 1.5 meters or $5 \lambda_{De}$. The hydrogen shock F^+ is weaker and narrower, with the maximal electric field of about 0.42 V/m at time $t = 0.0031 \text{ s}$ and the width of 0.7 meters or $2.5 \lambda_{De}$. There are several reasons to believe that oscillatory wakes in the 1-D model are physical. First, simulations with different grid resolution demonstrate clear convergence if the grid cell size is $\Delta x < \lambda_{De} / 16$ (see Figure 13). Second, similar oscillatory wakes are reported both in experiments [e.g., *Taylor et al.*, 1970] and simulations [e.g., *White et al.*, 1974; *Kozlov and McKinstrie*, 2002]. The reason for these wakes is the dispersion of ion-acoustic waves. Eventually, a unipolar spike transforms into a wave packet with asymmetric envelope, in qualitative agreement with *Hirose et al.* [1978].

[46] It is interesting that the nonlinear waves in the magnetospheric simulation exhibit similar behavior at much lower parallel electric fields due to excessive numerical diffusion of the advection algorithm.

[47] The double layers observed in the simulations above appear as a transitional phenomenon only and do not become stationary, which does not contradict available theories. *Verheest* [1989] concluded that an ion-acoustic double layer in a plasma with multiple ion species is

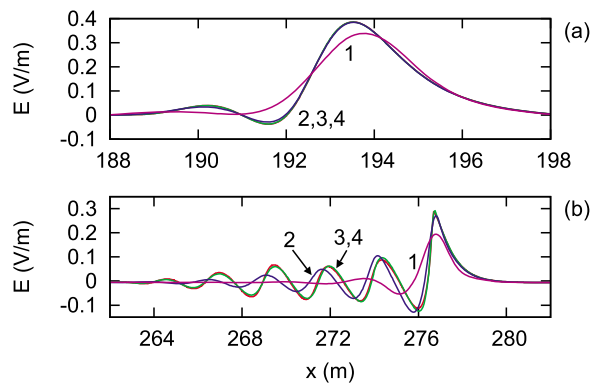


Figure 13. Convergence of Poisson simulations with different grid cell size. Detailed pictures of the electric field in the rightward-going (a) slow wave and (b) fast wave. These waves are labeled S^+ and F^+ in Figure 12, respectively. Curves 1, 2, 3, and 4 are obtained in simulations where the numerical grid has 4000, 8000, 16000, and 32000 cells, respectively, at time $t = 0.00648$ s.

impossible if all ion species are positive and there is only one electron population, which exactly matches the properties of the models discussed in the present paper. In order to obtain the double layer as a stationary propagating structure, one must either include both hot and cold electron populations [Reddy and Lakhina, 1991] or negatively charged ions [Mishra et al., 2002].

[48] Finally, the drop of the electrostatic potential across the whole area of an oxygen or a hydrogen shock wave is negligible both when the shock looks like a double layer (see the potential profile in the oxygen shocks S^{\pm} in Figure 12f) and when it looks like a short wave packet (see the potential profile in the hydrogen shocks F^{\pm} in Figure 12f). Therefore, the ion-acoustic shock waves are not effective for auroral particle acceleration.

5. Summary

[49] The nonlinear Lorentz force of a standing Alfvén wave in the ionospheric Alfvén resonator (IAR) compresses and rarefies the plasma along the geomagnetic field. With finite electron temperature, the density modification amplifies the parallel electric field in proportion to the electron pressure gradient. Ions with different mass respond differently to this electric field, which produces spatially separated local enhancements of light (hydrogen) and heavy (oxygen) ions. These perturbations propagate as ion-acoustic waves, and their amplitude grows due to the process of nonlinear wave steepening similar to shock tubes.

[50] An oxygen (hydrogen) density perturbation evolves into an oxygen (hydrogen) compressional shock wave: the oxygen (hydrogen) ion density is bigger behind the shock and it changes in a jump-like manner across the shock front, the shock propagates upward with the speed of a slow (fast) ion-acoustic wave. In the shock's frame, the incoming oxygen (hydrogen) flow in front of the shock is supersonic, behind the shock it is subsonic.

[51] Initially, the ion-acoustic shock waves in the IAR were obtained in numerical simulation with a 2-D multifluid model of low-altitude auroral flux tubes. This model de-

scribes large-scale motion of near-Earth plasma on a coarse grid using an algorithm which is not the best for description of sharp discontinuities. Simulations with the 2-D model have to be stopped at an early stage of the nonlinear steepening process in order to prevent the appearance of numerical artifacts. Therefore, a 1-D Poisson shock-capturing multifluid code was applied to simulate a relatively short ($1000\lambda_{De}$) plasma system with fine resolution ($\lambda_{De}/32$) and provide a detailed picture of evolution of the shock waves.

[52] The 1-D Poisson simulation confirms the formation of hydrogen and oxygen ion-acoustic shock waves from a density perturbation caused by converging plasma flows. It is found that a shock wave starts as a double layer, with a unidirectional electric field. At this stage, the maximal electric field for the selected plasma parameters is about 0.4–0.7V/m and the width of the shock is $2\text{--}5\lambda_{De}$. The double layer, however, decays into an intense ion-acoustic wave packet with an asymmetric, rapidly increasing and gradually decreasing envelope. The shocks appeared to be not suitable for particle acceleration neither when they look like double layers, nor when they transform into the wave packets.

[53] Finally, a perturbation growing into an ion-acoustic shock wave may be created not only by a standing Alfvén wave in the IAR, but by other mechanisms. There are satellite observations of intense ion-acoustic wave packets in the plasma sheet, well outside the IAR area [Cattell et al., 1998]. The nonlinear steepening will occur if, first, the perturbation is sufficiently strong. In the IAR model, for example, shock waves form when the amplitude of the transverse electric field of the driving Alfvén wave packet is no less than 0.12V/m, which is a high but not an unrealistic value. The second requirement is that the electron temperature must be much higher than the ion temperature, which probably limits application of this mechanism to altitudes above 2000 km. Inside the IAR, density perturbations at these altitudes may be produced by the resonator harmonics with higher numbers.

[54] **Acknowledgments.** The present study was supported by the Canadian Space Agency (CSA) and the National Sciences and Engineering Research Council of Canada (NSERC).

[55] Robert Lysak thanks Joachim Vogt and another reviewer for their assistance in evaluating this paper.

References

- Andersen, H. K., N. D'Angelo, P. Michelsen, and P. Nielsen (1967), Investigation of Landau-damping effects on shock formation, *Phys. Rev. Lett.*, *19*, 149–151.
- Boris, J. P., and D. L. Book (1973), Flux-corrected transport. I. SHASTA, a fluid transport algorithm that works, *J. Comput. Phys.*, *11*, 38–69.
- Bostrom, R., G. Gustafsson, B. Holback, G. Holmgren, and H. Koskinen (1988), Characteristics of solitary waves and weak double layers in the magnetospheric plasma, *Phys. Rev. Lett.*, *61*, 82–85.
- Carlson, R. E., and F. N. Fritsch (1985), Monotone piecewise bicubic interpolation, *SIAM J. Numer. Anal.*, *22*, 386–400.
- Cattell, C., J. Wygant, J. Dombeck, F. S. Mozer, M. Temerin, and C. T. Russell (1998), Observations of large amplitude parallel electric field wave packets at the plasma sheet boundary, *Geophys. Res. Lett.*, *25*, 857–860.
- Chaston, C. C., J. W. Bonnell, C. W. Carlson, J. P. McFadden, R. E. Ergun, R. J. Strangeway, and E. J. Lund (2004), Auroral ion acceleration in dispersive Alfvén waves, *J. Geophys. Res.*, *109*, A04205, doi:10.1029/2003JA010053.

- Dombeck, J., C. Cattell, J. Crumley, W. K. Peterson, H. L. Collin, and C. Kletzing (2001), Observed trends in auroral zone ion mode solitary wave structure characteristics using data from Polar, *J. Geophys. Res.*, *106*, 19,013–19,021.
- Dovner, P. O., A. I. Eriksson, R. Bostrom, and B. Holback (1994), Freja multiprobe observations of electrostatic solitary structures, *Geophys. Res. Lett.*, *21*, 1827–1830.
- Ergun, R. E., et al. (1998), FAST satellite wave observations of electric field structures in the auroral zone, *Geophys. Res. Lett.*, *25*, 2025–2028.
- Ergun, R. E., C. W. Carlson, J. P. MacFadden, F. S. Mozer, and R. J. Strangeway (2000), Parallel electric fields in discrete arcs, *Geophys. Res. Lett.*, *27*, 4053–4056.
- Erkaev, N. V., V. S. Semenov, V. A. Shaidurov, D. Langmayr, H. K. Biernat, and H. O. Rucker (2001), Propagation of nonlinear slow waves produced by pressure pulses along the Io flux tube, *Adv. Space Res.*, *28*, 1481–1488.
- Foster, J. C., C. del Pozo, K. Groves, and J.-P. St.-Maurice (1988), Radar observations of the onset of current driven instabilities in the topside ionosphere, *Geophys. Res. Lett.*, *15*, 160–163, doi:10.1029/GL015i002p00160.
- Fried, B. D., R. B. White, and T. K. Samec (1971), Ion acoustic waves in a multi-ion plasma, *Phys. Fluids*, *14*, 2388–2392.
- Hirose, A., O. Ishihara, S. Watanabe, and H. Tanaka (1978), Response of ion acoustic waves to an impulse, *Plasma Phys.*, *20*, 1179–1184.
- Hudson, M. K., and F. S. Mozer (1978), Electrostatic shocks, double layers, and anomalous resistivity in the magnetosphere, *Geophys. Res. Lett.*, *5*, 131–134, doi:10.1029/GL005i002p00131.
- Kletzing, C. A., F. S. Mozer, and R. B. Torbert (1998), Electron temperature and density at high latitude, *J. Geophys. Res.*, *103*, 14,837–14,845.
- Kozlov, M. V., and C. J. McKinstrie (2002), Sound waves in two-ion plasmas, *Phys. Plasmas*, *9*, 3783–3793.
- Landau, L. D., and E. M. Lifshitz (1987), *Fluid Mechanics, Course Theor. Phys.*, 2nd ed., Pergamon Press, New York.
- Mishra, M. K., A. K. Arora, and R. S. Chhabra (2002), Ion-acoustic compressive and rarefactive double layers in a warm multicomponent plasma with negative ions, *Phys. Rev. E*, *66*, 046402.
- Montgomery, D. (1967), Evolution of a nonlinear ion acoustic wave, *Phys. Rev. Lett.*, *19*, 1465–1466.
- Mozer, F. S., C. A. Cattell, M. K. Hudson, R. L. Lysak, M. Temerin, and R. B. Torbert (1980), Satellite measurements and theories of low altitude auroral particle acceleration, *Space Sci. Rev.*, *27*, 155–213.
- Polyakov, S. V., and C. O. Rapoport (1981), Ionospheric alfvén resonator, *Geomagn. Aeron.*, *21*, 816.
- Prakash, M. (1997), Excitation of ion-acoustic turbulence and its role in auroral processes at Freja altitude, *Phys. Chem. Earth*, *22*, 773–776.
- Priestley, A. (1993), A quasi-conservative version of the semi-Lagrangian advection scheme, *Mon. Weather Rev.*, *121*, 621–629.
- Quon, B. H., and A. Y. Wong (1976), Formation of potential double layers in plasmas, *Phys. Rev. Lett.*, *37*, 1393–1396.
- Rambo, P. W., and J. Denavit (1991), Fluid and field algorithms for time-implicit plasma simulation, *J. Comput. Phys.*, *92*, 185–212.
- Reddy, R. V., and G. S. Lakhina (1991), Ion acoustic double layers and solitons in auroral plasma, *Planet. Space. Sci.*, *39*, 1343–1350.
- Rietveld, M. T., P. N. Collis, and J.-P. St.-Maurice (1991), Naturally enhanced ion acoustic waves in the auroral ionosphere observed with the EISCAT 933-MHz radar, *J. Geophys. Res.*, *96*, 19,291–19,305.
- Sato, T., and H. Okuda (1981), Numerical simulations on ion acoustic double layers, *J. Geophys. Res.*, *86*, 3357–3368.
- Seyler, C. E., J.-E. Wahlund, and B. Holback (1995), Theory and simulation of low-frequency plasma waves and comparison to Freja satellite observations, *J. Geophys. Res.*, *100*, 21,453–21,472, doi:10.1029/95JA02052.
- Staniforth, A., and J. Cote (1991), Semi-Lagrangian integration schemes for atmospheric models—A review, *Mon. Weather Rev.*, *119*, 2206–2223.
- Sydorenko, D., R. Rankin, and K. Kabin (2008), Nonlinear effects in the ionospheric Alfvén resonator, *J. Geophys. Res.*, *113*, A10206, doi:10.1029/2008JA013579.
- Taylor, R. J., D. R. Baker, and H. Ikezi (1970), Observation of collisionless electrostatic shocks, *Phys. Rev. Lett.*, *24*, 206–209.
- Temerin, M., K. Cerny, W. Lotko, and W. S. Mozer (1982), Observations of double layers and solitary waves in the auroral plasma, *Phys. Rev. Lett.*, *48*, 1175–1179.
- Verheest, F. (1989), Ion-acoustic double layers in multi-species plasmas maintained by negative ions, *J. Plasma Phys.*, *42*, 395–406.
- Wahlund, J.-E., F. R. E. Forme, H. J. Opgenoorth, M. A. L. Persson, E. V. Mishin, and A. S. Volokitin (1992), Scattering of electromagnetic waves from a plasma: enhanced ion acoustic fluctuations due to ion-ion two-stream instabilities, *Geophys. Res. Lett.*, *19*, 1919–1922.
- Warmuth, A. (2007), Large-scale waves and shocks in the solar corona, *Lect. Notes Phys.*, *725*, 107–138.
- White, R. B., B. D. Fried, and F. V. Coroniti (1974), Formation of ion-acoustic shocks, *Phys. Rev. Lett.*, *17*, 211–214.

K. Kabin, Department of Physics, Royal Military College of Canada, PO Box 17000 STN Forces, Kingston, ON K7K7B4, Canada. (konstantin.kabin@rmc.ca)

R. Rankin and D. Sydorenko, Department of Physics, University of Alberta, Room 238 CEB, 11322 - 89 Ave., Edmonton, AB T6G 2G7, Canada. (rrankin@ualberta.ca; sydorenk@ualberta.ca)